The supplementary information for the paper:

Improvement of the perovskite photodiodes performance via advanced interface engineering with polymer dielectric

A.P. Morozov[1§], L.O. Luchnikov[1§], S. Yu. Yurchuk[2], A.R. Ishteev[1], P.A. Gostishchev[1], S.I. Didenko[2], N.S. Saratovsky[3], D.O. Balakirev[3], I.V. Dyadishchev[3], A.A. Romanov[2], E.A. Ilicheva[1], A.A. Vasilev[2], S.S. Kozlov[4], D.S. Muratov[5*], Yu. N. Luponosov[3*] and D.S. Saranin[1*]

[1]LASE – Laboratory of Advanced Solar Energy, NUST MISiS, 119049 Moscow, Russia
[2]Department of semiconductor electronics and device physics, NUST MISiS, 119049 Moscow, Russia
[3]Enikolopov Institute of Synthetic Polymeric Materials of the Russian Academy of Sciences (ISPM RAS), Profsoyuznaya St. 70, Moscow, 117393, Russia

[4]Laboratory of Solar Photoconverters, Emanuel Institute of Biochemical Physics, Russian Academy of Sciences, 119334 Moscow, Russia

[5]Department of Chemistry, University of Turin, 10125, Turin, Italy

§: The authors contributed equally to this work

Experimental section:

Materials

All organic solvents—dimethylformamide (DMF), N-Methylpyrrolidone (NMP), isopropyl alcohol (IPA), chlorobenzene (CB) were purchased in anhydrous, ultra-pure grade from Sigma Aldrich, and used as received. P(VDF-TrFE) (70:30 mol%) was purchased from Sigma Aldrich. The preparation of P(VDF-co-CTFE)-graft-PEMA has been previously described[1]. Ethylacetate (EAC, 99+% purity) was purchased from Reaktivtorg-Himprocess hps, 2-Methoxyethanol was purchased from Acros Organics (99.5+%, for analysis), HNO_3 (70%). Photodiodes were fabricated on In_2O_3: SnO_2 (ITO) coated glass (R_{sheet}<7 Ohm/sq) from Zhuhai Kaivo company (China). $NiCl_2 \cdot 6H_2O$ (from ReaktivTorg 99+% purity) used for HTM fabrication. Lead Iodide (99.9%), Cesium iodide (99.99%), Cesium chloride (99.99%) trace metals basis from LLC Lanhit, Russia and formamidinium iodide (FAI, 99.99% purity from GreatcellSolar), were used for perovskite ink. [6,6]-Phenyl-C61-butyric acid methyl ester (99% purity) was purchased from MST NANO (Russia). Bathocuproine (BCP, >99.8% sublimed grade) was purchased from Osilla Inc. (UK) and used for the fabrication of hole blocking layer.

Inks preparation

For the preparation of composition $Cs_{0.2}FA_{0.8}PbI_{2.93}Cl_{0.07}$ perovskite ink, we used CsCl, CsI, FAI, PbI_2 powders in a 0.07:0.13:0.8:1 molar ratio. The resulting mixture was dissolved in a DMF:NMP (volume ratio 640:360) with a concentration of 1.35 M and stirred at a temperature of 50 °C for 1 h. PCBM was dissolved in CB at a concentration of 27 mg/ml and stirred for 1 h at a temperature of 50 °C. BCP was dissolved in IPA at a concentration of 0.5 mg/ml and stirred for 8 h at a temperature of 50 °C. Before use, all solutions were filtered through 0.45 μm PTFE filters. P(VDF-TrFE) was dissolved in a perovskite solution at a concentration of 5×10^{-3} mg/ml. For bulk/n-side configuration P(VDF-TrFE) was dissolved in EAC with DMF (volume ratio 200:1) at a concentration of 5×10^{-3} mg/ml and stirred for 1 h at a temperature of 50 °C

Device fabrication

Perovskite photodiodes were fabricated with inverted planar architecture ITO/c-NiO /perovskite ($Cs0.2FA0.8PbI_{2.93}Cl_{0.07}$)/PCBM/BCP/Cu. Firstly, the patterned ITO substrates were cleaned with detergent, de-ionized water, acetone, and IPA in the ultrasonic bath. Then, substrates were activated under UV-ozone irradiation for 30 min. $NiCl_2 \cdot 6H_2O$ precursor for NiO HTM film was spin-coated at 4000 RPMs (30 s), dried at 120 °C (10 min), and annealed

at 300 °C (1 h) in the ambient atmosphere. Perovskite absorber film was crystallized on the top of HTM with solvent engineering method. Perovskite precursor was spin-coated at 3000 RPMs (5 s), and 5000 RPMs (30 s), 200 μL of EAC were poured on the substrate on the 21st second after the start of the rotation process. Then, substrates were annealed at 85 °C (1 min) and 105 °C (30 min) for conversation into the black perovskite phase. Deposition process of perovskite with P(VDF-TrFE) addition was the same. For bulk/n-side configuration PVDF was spin-coated upon annealed perovskite film at 4000 RPMs (30s) and annealed at 105 °C (5 min). The PCBM ETL was spin-coated at 4000 RPMs (30 s) and annealed at 50 °C (5 min). BCP interlayer was also spin-coated at 4000 RPMs (30 s) and annealed at 50 °C (5 min). The copper cathode was deposited with the thermal evaporation method at 2×10^{-6} Torr vacuum level. All devices were encapsulated with UV epoxy from Osilla inc. UV LS processes (P1-P3) were described in the manuscript.

Laser scribing

The laser scriber system was designed by LLC Nordlase (Russia).

Laser type – Nd:YVO_4, 355 nm, impulse – 22 ns at 50kHz. Maximum power – 3W.

The positioning of the samples was realized using motorized XY stage from Standa (1 um resolution in XY movement).

The maximum attenuation of the system – 99%.

During scribing all substrates were fixed with vacuum chuck.

Laser patterning cycle

ITO scribing (P1) was performed using 3 W power at a rate of 5 mm/s (50 kHz, 1 pulse per 3 microns). Electrical isolation between the anode electrodes of the ITO for each pixel in the row was achieved by sequentially conducting 9 passes of the laser beam (50-micron diameter) with an offset of 10 microns.

The P2 process was realized in three passes (5 μm offset) at 1 W power at a speed of 5 mm/s. The width of the scribing line of the P2 process was ~60 μm. After deposition of the metal electrode in a vacuum, the P3 process required the removal of conductive material from the insulating zones between the ITO anode electrodes. Additionally, transverse scribing of the metal electrode was performed to form the final pixel geometry.

The pixel formation, indicated by the transverse metal scribing line in Fig. 2(a) in the manuscript, required the process to be performed at 1 W power, a speed of 2 mm/s, and three passes (10 μm offset). The width of the cut was 40 μm. Electrical isolation between pixels (P3 process) was achieved by ablating the metal contact using the P1 path (side isolation lines according to the top view in Fig. 2(a)). To ensure isolation, scribing was performed at a power of 3 W, speed of 20 mm/s for 1 pass of the laser beam with a cutting width of 40 μm. The P1-P3 patterning processes were the same for PPDs of all configurations.

Characterization

Surface roughness and film thicknesses were measured with KLA-Telencor stylus profilometer.

The fluorescence was induced with 375 nm picosecond pulsed laser (CNILaser MDL-PS-375). The signal acquisition was conducted until 15000 counts.

$$\alpha(h\nu) = \frac{B(h\nu - E_g)^{\frac{1}{2}}}{h\nu} \quad \text{(S1)}$$

Where α - absorption coefficient;

h – Plank's constant;

ν – frequency;

E_g – band gap.

KPFM measurements were conducted using an NT-MDT Ntegra AFM equipped with conductive probe NSG03/Au (NT-MDT). The work function was determined with a fresh HOPG surface serving as the energy baseline. The surface topography scans carried in tapping mode first and then a 1 V voltage was applied on the sample with tip resonance frequency (~200 kHz) to measure the sample surface potential (V_{CPD}) distribution through a DC voltage feedback loop. The scan rate was set to 0.8 Hz, and a lift scan height of approximately 50 nm was adopted. The work function (W_f) was calculated according to S1 and S2.

$$W_f^{tip} = W_f^{HOPG} - V_{CPD}^{HOPG} \quad \text{(S2)}$$

$$W_f^{sample} = W_f^{tip} - V_{CPD}^{sample} \quad \text{(S3)}$$

X-ray diffraction (**XRD**) patterns was measured with X-ray diffractometer Tongda TDM-10 using CuKα as a source with wavelength 1.5409 Å under 30 kV voltage and a current of 20 mA.

Steady state photoluminescence (**PL**) measurements were performed on Cary EclipseFluorescence Spectrophotometer with an excitation wavelength of550 nm. Absorption spectra were measured on Spectronic HeliosAlpha UV–vis spectrophotometer from Thermo Fisher Scientific (Waltham, MA, USA). The Tauc plots calculation was realized using equation:

The dark JV-curves measurements were performed in the dark box in an ambient atmosphere with Keithley 2400 SMU in 4-wire mode (voltage step of 20 mV).

We used TDS-P003L4F07- LED (540 nm) as a light source for estimation of V_{oc}, J_{sc} vs. P_0. The output parameters (V_{oc}, J_{sc}) were extracted from JV curves measured with Keithley 2400 SMU in 4-wire mode and a settling time of 10^{-2} s. The LED was connected to a GW Instek PSP-603 source in a hinge-mounted configuration. Optical power measurements were performed on a ThorLabs S425C. Illuminance measurements were performed on a UPRtek MK350. Completed set up for characterization of PPDs was placed in a black box.

The dynamic response and f_{3dB} was measured with Tektronix TDS 3054C (oscilloscope) and Tektronix AFG 3252 (pulse generator). We used TDS-P001L4G05 STAR LED (540 nm) as a light source. Completed set up for characterization of PPDs was placed in a black box.

The **PPD**s stability was assessed by the change in response speed after heating for 250 hours at a temperature of 70 °C. Data was obtained for 30 PPDs of each configuration.

The **EQE** spectra were measured using QEX10 solar cell quantum efficiency measurement system (PV Measurements Inc., USA) equipped with xenon arc lamp source and dual grating monochromator. Measurements were performed in DC mode in the 300–850 nm range at 10 nm step. The system was calibrated using the reference NIST traceable Si photodiode.

Time resolved photoluminescence **(TRPL)** measurements was performed with time correlated single photon counter technique (TCSPC) on Zolix OmniFluo-990 spectrofluorometer.

PIVTS & AS

In this work, we used a 470 nm, 250 mW/cm² LED with a 2 s light pulse duration to implement the Photo-induced Voltage Transient Spectroscopy (PIVTS) technique. To verify the presence of mobile ions, we also performed Admittance Spectroscopy (AS). Notably, the high-power illumination was done through the optical window of the cryostat. Such measurements are particularly sensitive to device active layer properties and its effect of mobile ions. High concentration of mobile charged defects can screen build-in of applied fields on the Debye length scale, leading to device structure capacitance changes:($C = \frac{\epsilon\epsilon_0 A}{L_D}$, $L_D = \sqrt{\frac{\epsilon\epsilon_0 k_B T}{q^2 N_i}}$). The same approach used for determining times and frequencies for such defects will follow applied bias. For given diffusion, the coefficient D time of mobile ion will move

across L_D will be: ${L_D^2}/{D} = \tau$. So the condition of peak in AS will be: $\omega \cdot \tau = 1 \Rightarrow \tau = \frac{\epsilon\epsilon_0 k_B T}{q^2 N_i D_0} \exp\left(\frac{E_A}{k_B T}\right)$, and then E_A and D_0 can be determined from the Arrhenius plot.

Fourier-transform infrared (FTIR) spectroscopic studies were carried out on a Varian Scimitar 2000 FTIR instrument with a maximum resolution of 0.5 cm^{-1}

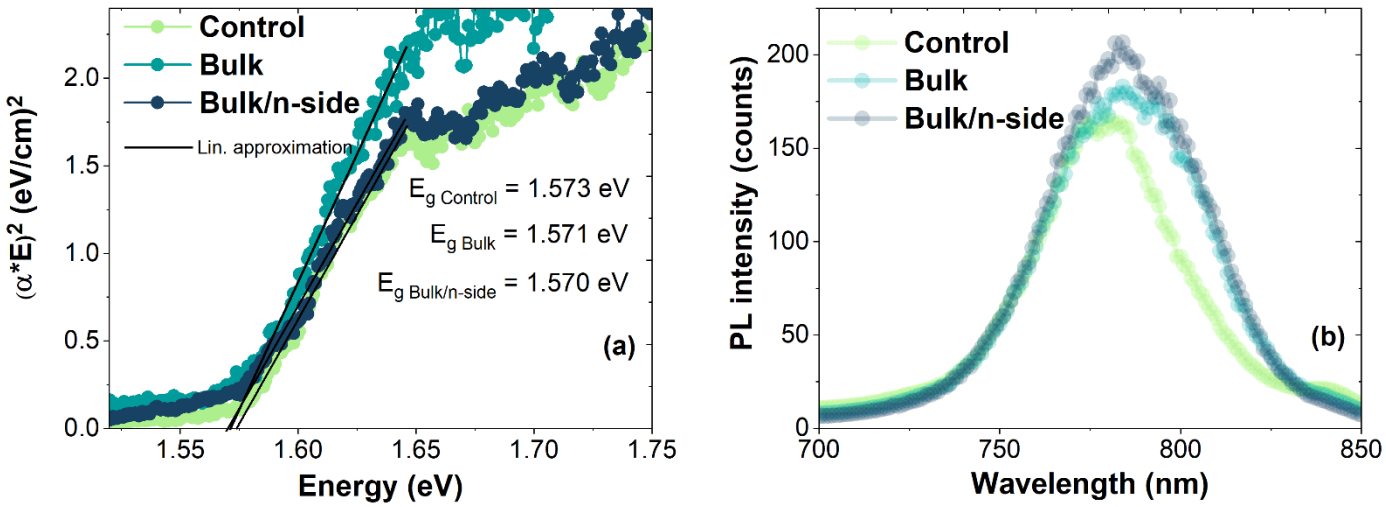

Figure S1 – Absorption spectra (a) and PL spectra (b) of fabricated thin-film samples with dielectric interlayers

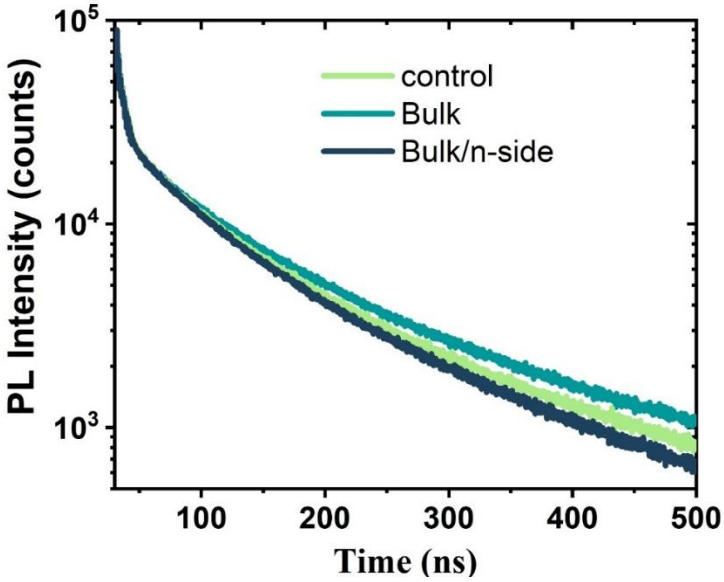

Figure S2 – The TRPL spectra of the PPDs with dielectric interlayers

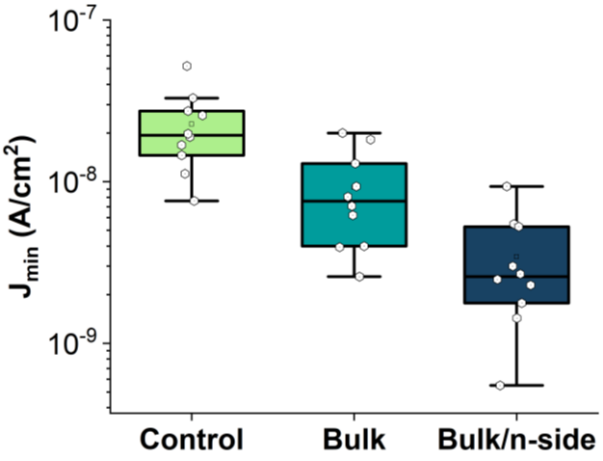

Figure S3- Box-charts of dark J_{min} values for PPDs with P(VDF-TrFE)

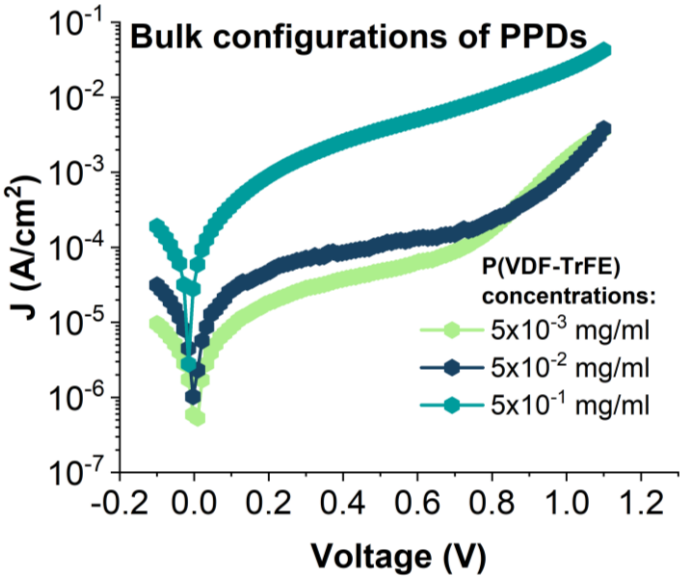

Figure S4 – The dark JVs of PPDs fabricated with various concentrations of P(VDF-TrFE)

Details for the double diode model used for fitting of dark JV curves

The equation for the diode current-voltage curve, including series (Rs) and shunt (Rsh) resistance, has the following expression (S1):

$$J = J_0 \cdot \left(\exp\left(\frac{q(V - J \cdot R_s)}{m \cdot k \cdot T} \right) - 1 \right) + \frac{V - J \cdot R_s}{R_{sh}} . \quad \text{(S4)}$$

For common pn junction, such a model describes the characteristics of real structures quite accurately. However, for a p-i-n structure, such a model does not always allow us to express the characteristic corresponding to experimental results. The reason for this is the presence of two barriers from the p- and n-

regions, therefore, to calculate the current-voltage characteristics of the p-i-n structure, we used a two-diode model, represented by the equivalent circuit in Fig. S2. [2]

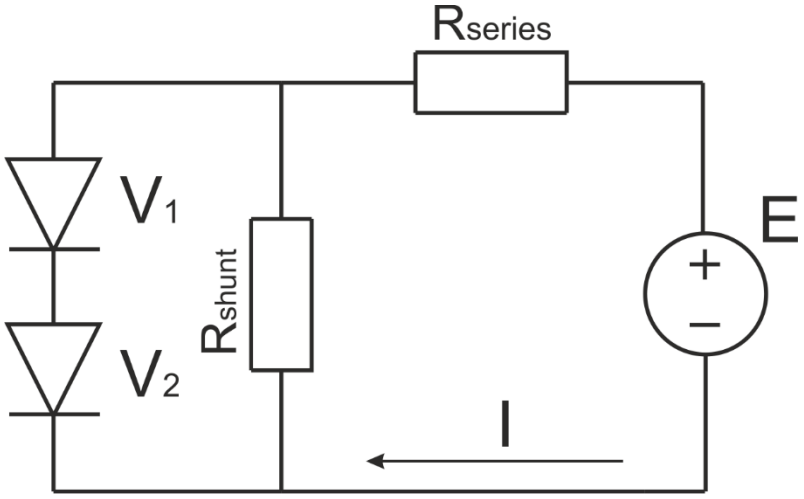

Figure S5 – Double diode circuit for modeling of pin PSC

Diodes 1 and 2 in this circuit are ideal diodes, the current-voltage characteristics of which are described by the expressions S2-S3:

$$J_1 = J_{01} \cdot \left(\exp\left(\frac{qV_1}{m_1 \cdot k \cdot T} \right) - 1 \right) \tag{S5}$$

$$J_2 = J_{02} \cdot \left(exp\left(\frac{qV_2}{m_2 \cdot k \cdot T} \right) - 1 \right) \tag{S6}$$

Two diode structures are connected in series, so the currents are equal to each other.

$$J_d = J_{01} \cdot \left(\exp\left(\frac{qV_1}{m_1 \cdot k \cdot T} \right) - 1 \right) = J_{02} \cdot \left(\exp\left(\frac{qV_2}{m_2 \cdot k \cdot T} \right) - 1 \right) \tag{S7}$$

Since the equivalent circuit is branched, it is necessary to solve a system of equations obtained from Kirchhoff's laws to calculate the current-voltage characteristic, For a given voltage V, unknown values are the currents in the diode and shunt resistance circuits J_d and Rsh. The voltages applied to each diode V_1 and V~~2~~, and the total current J, which we must find for each given voltage. The system of equations (S4) - (S7) is sufficient for the numerical calculation of the current – voltage characteristics according to the two-diode model, but it is necessary to calculate the model parameters: leakage currents of each individual diode J_{01} and J_{02}, non-ideality coefficients m_1 and m_2 of each diode, series resistance *Rs* and shunt resistance *Rsh*.

$$V_1 + V_2 = V - J \cdot R_s , \tag{S8}$$

$$J_{R_{sh}} = \frac{V - J \cdot R_s}{R_{sh}} , \tag{S9}$$

$$J = J_d + J_{R_{sh}}\,. \tag{S10}$$

The calculation was done with one of the methods for multi-parameter optimization, in which the objective function requiring minimization of the sum for the differences between the experimental and theoretically calculated currents (S8).

$$\sum_{i=1}^{m}\left(J_{ex_i} - J_{teor_i}\right)^2, \tag{S11}$$

where m is the number of experimental points.

Calculation program was developed in Borland Delphi 7, which allows determining the parameters of a two-diode structure using multi-parameter optimization by the coordinate descent method.

$$R = \frac{I_{ph}}{P_0} \tag{S12}$$

Where I_{ph}- photocurrent (A)

P_0- power of the illumination (W)

$$LDR = 20\log\left(\frac{I_{ph}}{I_D}\right) \tag{S13}$$

Where I_{ph}- photocurrent in linear range

I_D- dark current

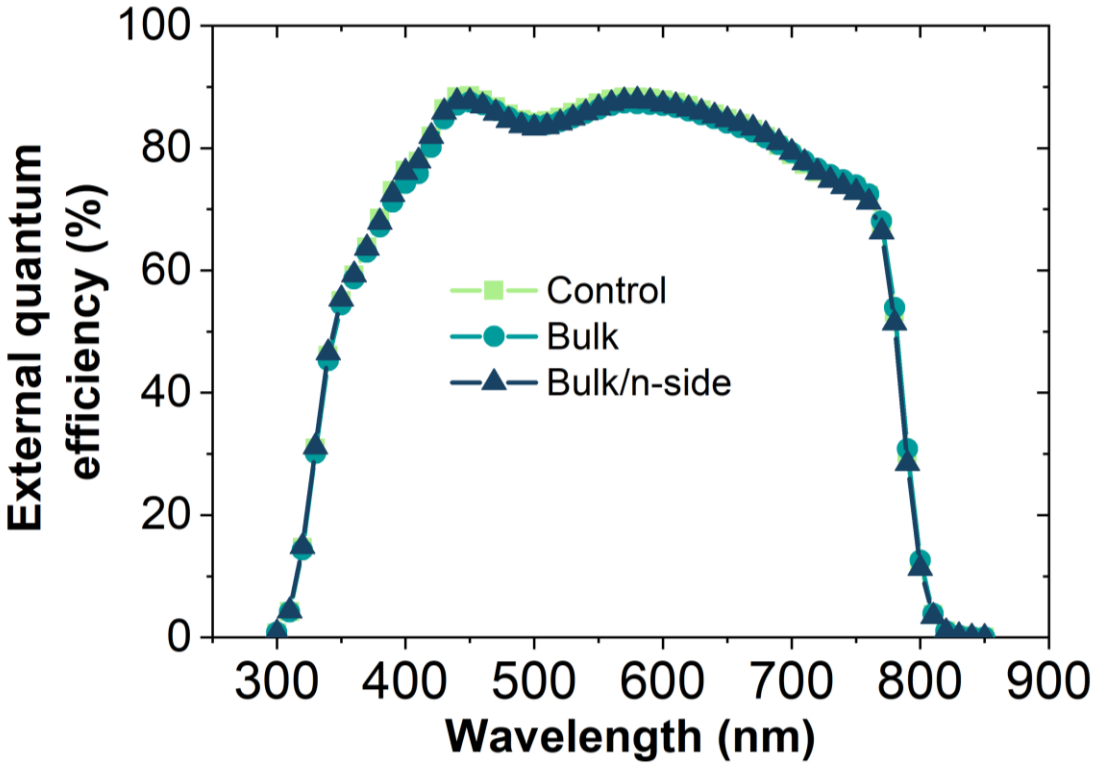

Figure S6 – The external quantum efficiency of the PPDs with dielectric interlayers

$$D^* = \frac{I_{ph}\sqrt{A}}{P_0}\left(\frac{1}{(2qJ_d)^{1/2}}\right) \tag{S14}$$

Where A – active area of the device

$$NEP = \frac{(2qJ_d)^{1/2}}{R} \tag{S15}$$

Table S1 – State-of-the art performance in PPDs

Architecture	**Specific Detectivity (Jones)**	**Wavelength (nm)**	**Response Time (Rise/Fall)**	**NEP (W/√Hz)**	**LDR (dB)**	**Link**
p-i-n Control	$2.20\cdot10^{11}$	540	6.3 us/10.9 us	$1.76\text{x}10^{-12}$	76.6	This work
p-i-n Bulk	$5.78\cdot10^{11}$	540	4.9 us/6.7 us	$6.65\text{x}10^{-13}$	92.0	This work
p-i-n Bulk/n-side	$9.69\cdot10^{11}$	540	4.6 us/6.5 us	$4.00\text{x}10^{-13}$	99.5	This work
p-i-n	1.5×10^{13}	600	48 us/ 35 us	N/A	N/A	[3]
n-i-p	7×10^{12}	600	2.9 us/2.9 us	1.88×10^{-13}	172.7	[4]

p-i-n	3.8×10^{12}	800	7.2 us/ 14.4 us	N/A	N/A	[5]
n-i-p	1.4×10^{12}	300–800	6 us/ 12 us	N/A	N/A	[6]
p-i-n	1.8×10^{12}	420	2.1 us/5.3 µs	N/A	N/A	[7]
n-i-p	1.3×10^{12}	600	150/240 µs	N/A	129	[8]
n-i-p	1.4×10^{12}	600	6 us/ 12 us	N/A	80	[9]
p-i-n	1.2×10^{13}	600	100 ns / 100 ns	N/A	N/A	[10]
n-i-p	1.35×10^{12}	310-420	2.1 µs / 5.3 µs	N/A	N/A	[11]
n-i-p	5.3×10^{10}	800	1.1 µs / 1.1 µs	N/A	90	[12]
n-i-p	8.91×10^{10}	340	30 ms / 35 ms	N/A	N/A	[13]
n-i-p	2×10^{13}	532	N/A	N/A	N/A	[14]
n-i-p	1.40×10^{14}	532	N/A	N/A	N/A	[15]
tandem	2×10^{15}	532	N/A	N/A	N/A	[16]

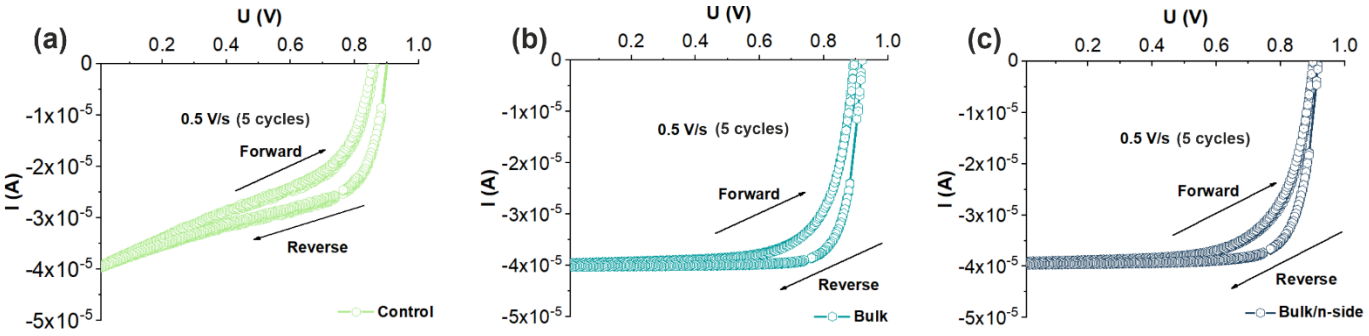

Figure S7 – IV hysteresis effects for various configurations of the fabricated PPDs

$$HI = \frac{P_{\max reverse} - P_{\max forrward}}{P_{\max reverse}} \qquad (S16)$$

Where $P_{max\ reverse}$ – value of the max power calculated for reverse scan;

$P_{max\ forward}$ – value of the max power calculated for reverse scan;

Table S2 – the HI for the fabricated PPDs

0.5 V/s	Control	Bulk	Bulk/n-side
1st cycle	0.14	0.08	0.11
3st cycle	0.21	0.16	0.16
5th cycle	0.23	0.15	0.16

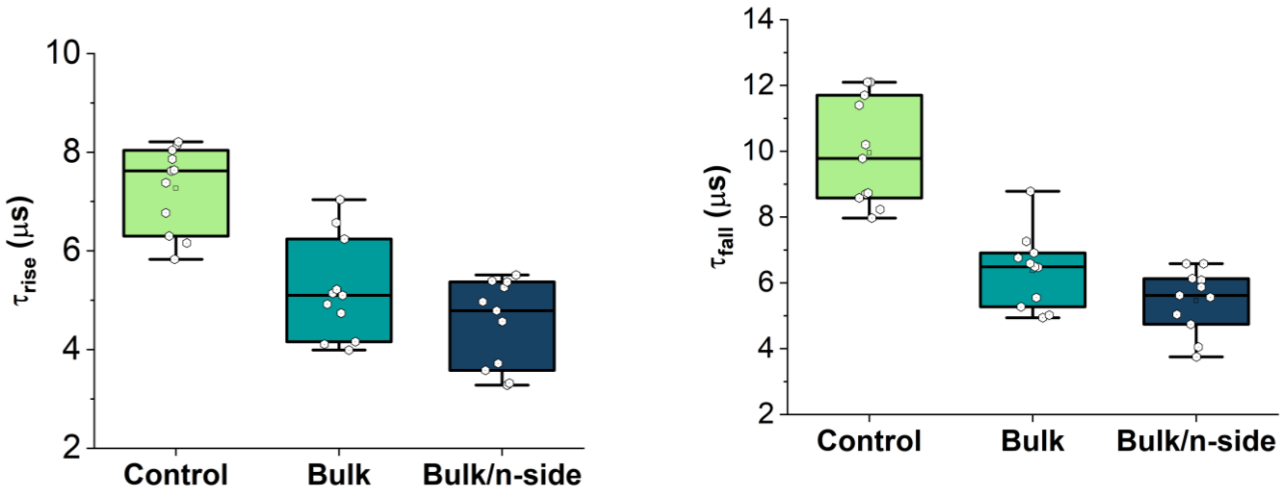

(a) (b)

Figure S8 - Box-charts of rise time (a) and fall time (b) values for PPDs with P(VDF-TrFE)

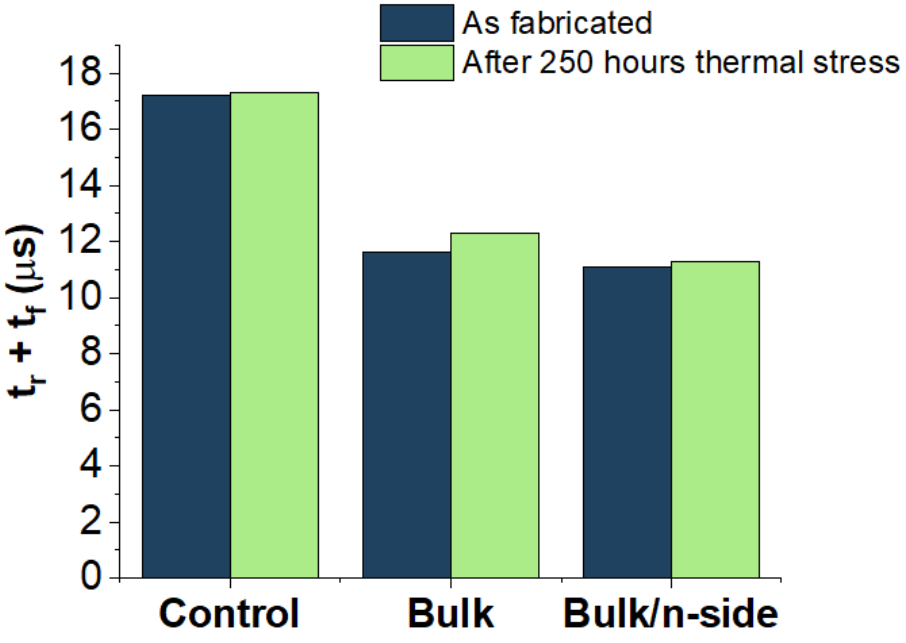

Figure S9 – Response speed of the devices before and after thermal stress

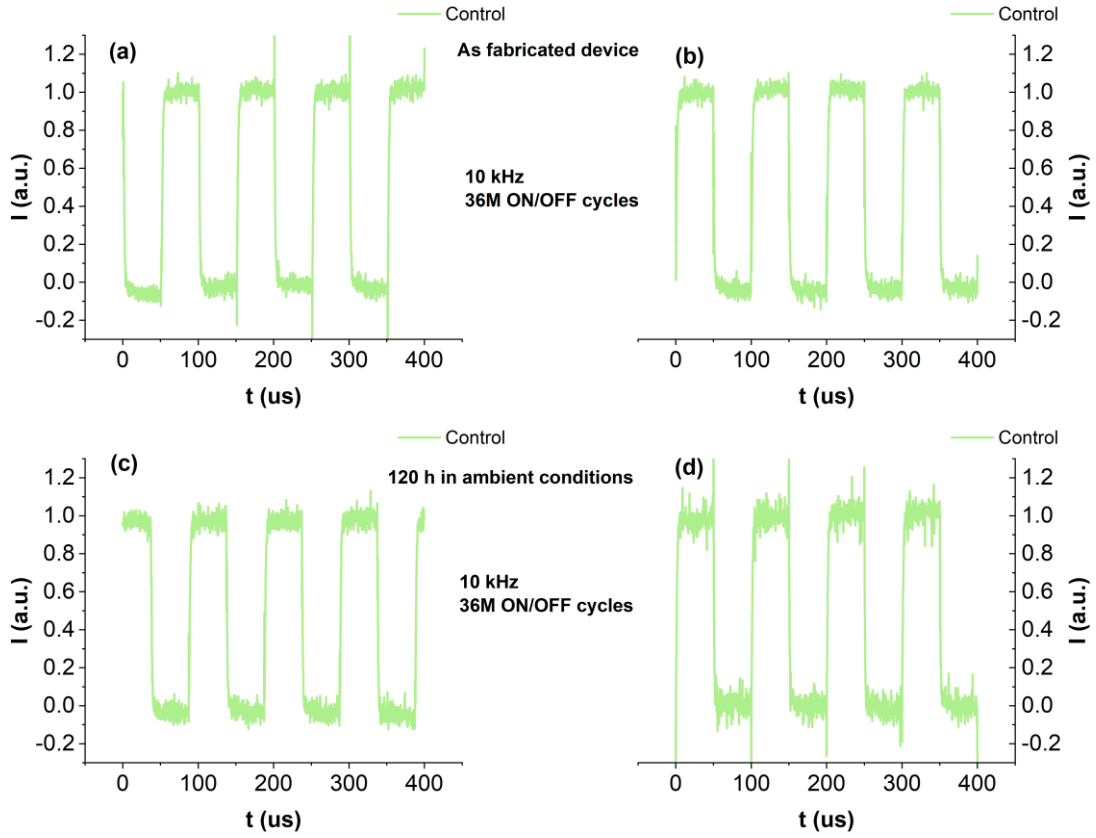

Figure S10 – The stability performance of the control PPDs before and after continuous ON/OFF cycling (a)(b) and storage under high-humidity conditions (c)(d)

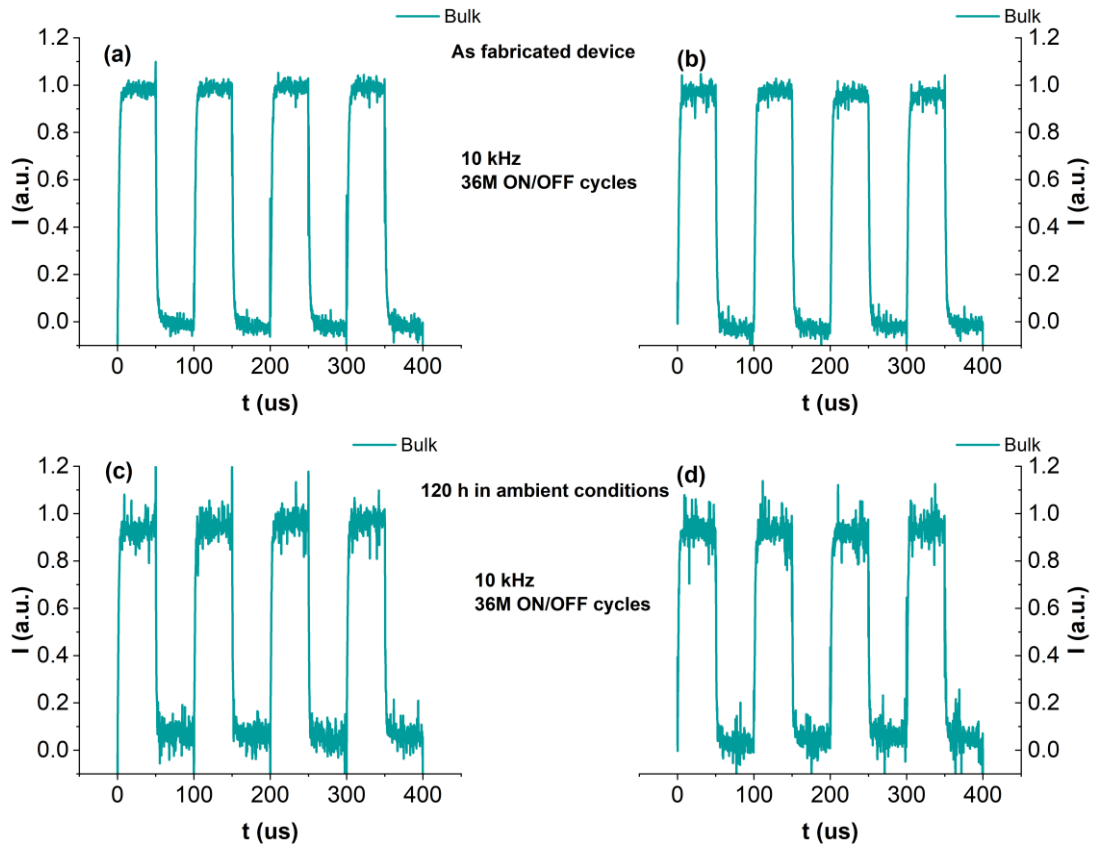

Figure S11 – The stability performance of the Bulk PPDs before and after continuous ON/OFF cycling (a)(b) and storage under high-humidity conditions (c)(d)

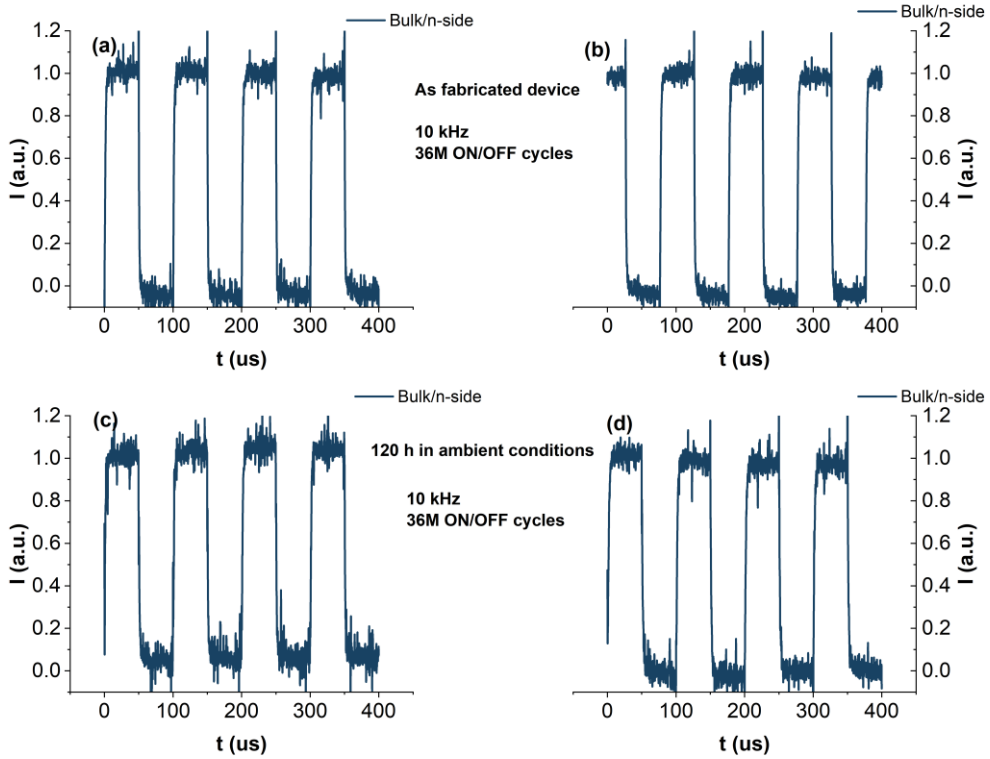

Figure S12 – The stability performance of the Bulk PPDs before and after continuous ON/OFF cycling (a)(b) and storage under high-humidity conditions (c)(d)

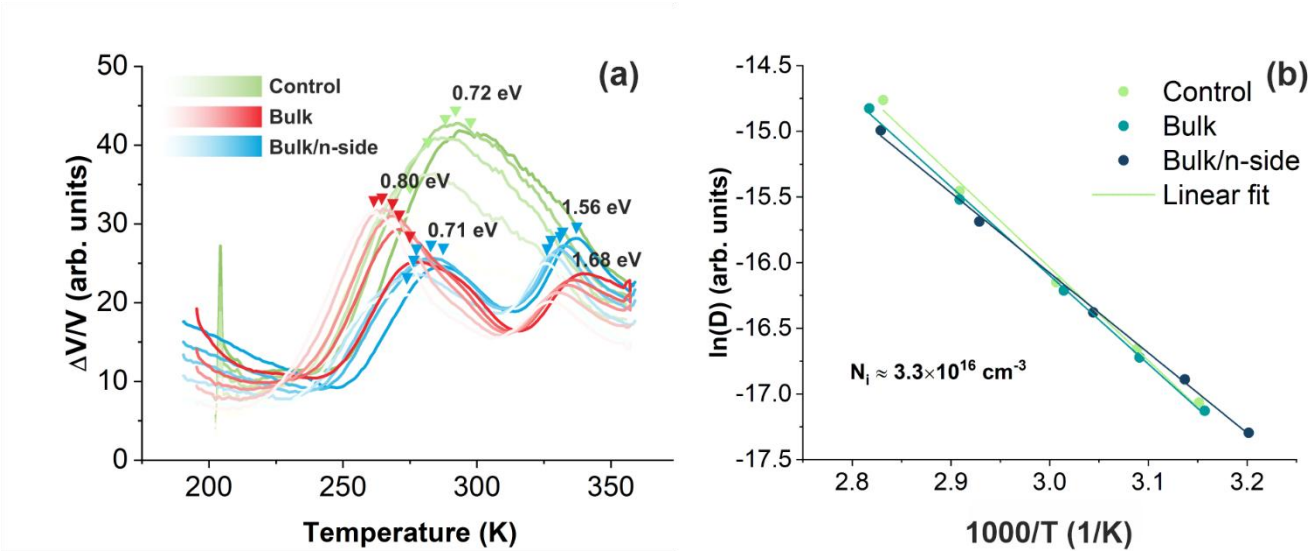

Figure S13 – The PIVTS measurements for the PPDs (a), admittance spectra for PPDs (b)

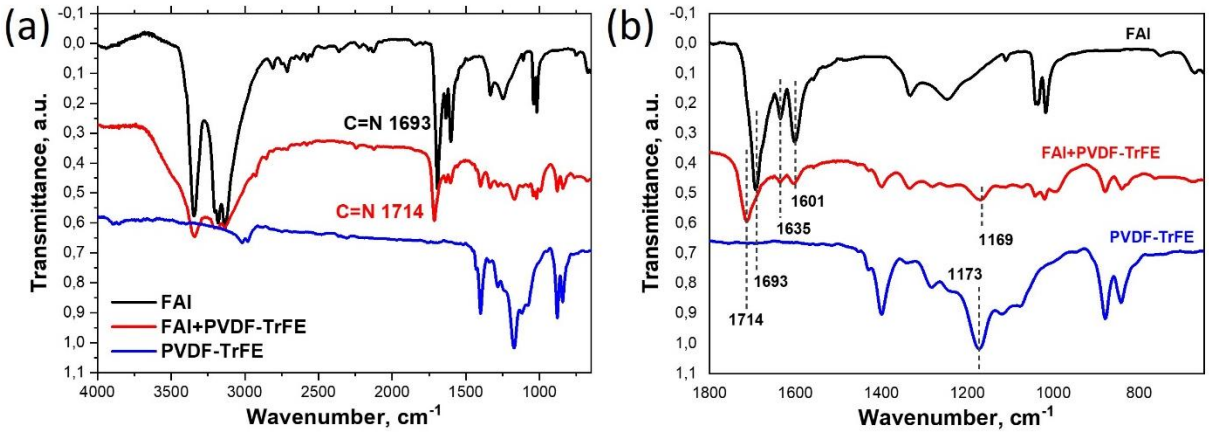

Figure S14 – FTIR spectra of fresh FAI, PVDF-TrFE, and their mixture (a); The zoomed interval from 1800 cm^{-1} to 650 cm^{-1} for the corresponding spectra (b)

The incorporation of PVDF-TrFE resulted in a notable shift of the characteristic peak for the partial double bond stretching of FAI to a higher wavenumber, from 1693 cm^{-1} to 1714 cm^{-1}. This is probably because the N–H···I hydrogen bond between FA+ and I− was weakened because of the addition fluorine-containing dielectric PVDF-TrFE. A comparable outcome has been documented in the study conducted in Ref.[17], wherein the introduction of hexafluorobenzene resulted in a reduction in the formation of defects in the resulting formamidinium lead halides.

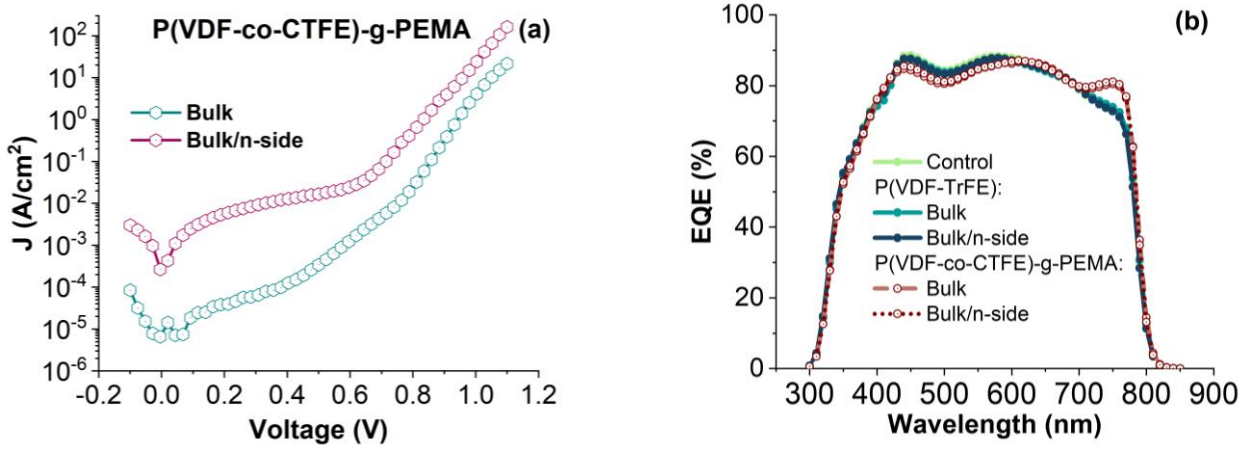

(a) (b)

Figure S15 – The dark JVs for the PPDs with P(VDF-co-CTFE)-g-PEMA (a), comparison of EQE spectra for PPDs with P(VDF-co-CTFE)-g-PEMA and P(VDF-TrFE)

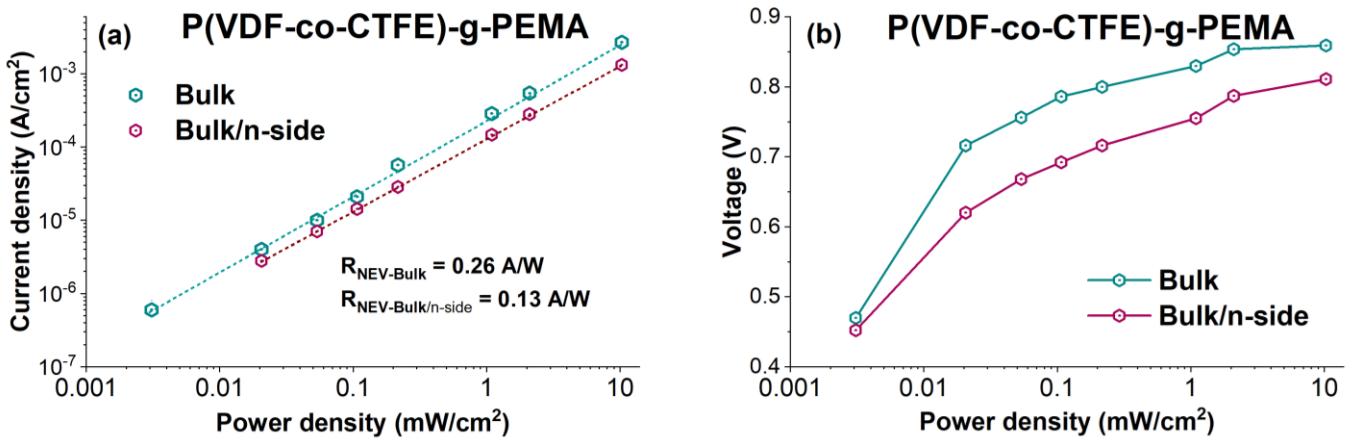

Figure S16 - The linearity plot of J_{sc} to P_0 for the various perovskites modifications with P(VDF-co-CTFE)-g-PEMA on a logarithmic scale (a); the dependence of V_{oc} vs. P_0 on a semi-logarithmic scale (b)

$$|I_{ph}| = \eta_{abs}\eta_{qe}\eta_{ce}\frac{q\lambda}{hc}I_L \qquad \text{(S17)(Zeiske et al., 2022)}$$

Where I_{ph}- photocurrent;

η_{abs}- absorptance;

η_{abs}- quantum efficiency for the photogenerated charge carriers;

η_{ce} -charge collection efficiency;

q – elementary charge;

λ- wavelength;

h-Planck's constant;

c – speed of light;

I_L- light intensity.

For testing PPDs in set-up with X-ray source we used the following equipment:

Rad-160 X-ray Source (Russia)

Maximum anode voltage 170 kV

Maximum anode current 1 mA

Maximum power at the tube anode, not less than 170 W.

CsI scintiliting bar (Fomos materials, Russia)

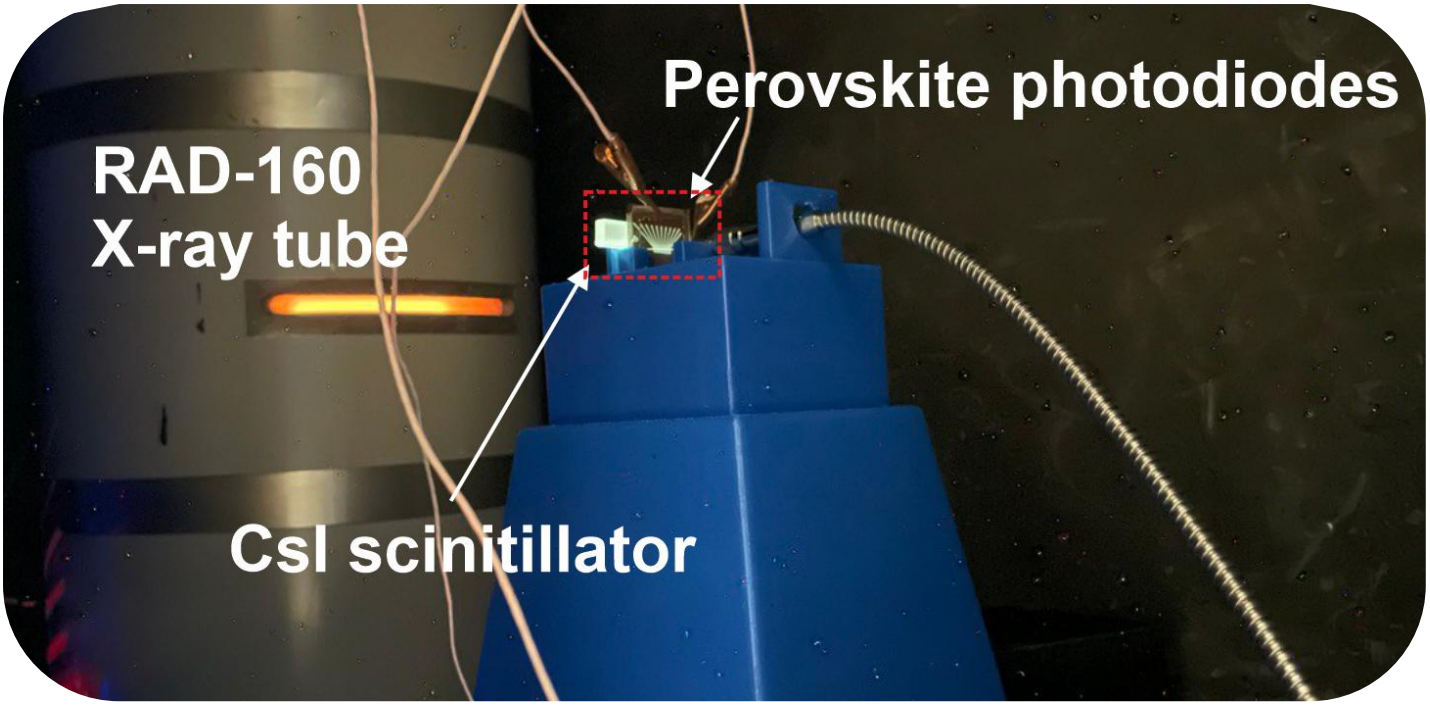

Figure S17 – The photo-image of the set-up with RAD 160 (W-based x-ray tube), CsI scintillator and perovskite photodiodes

References:

[1] E. A. Kleimyuk, A. I. Kosyakova, A. I. Buzin, V. G. Shevchenko, Yu. N. Luponosov, S. A. Ponomarenko, *Polymer Science, Series C* **2022**, *64*, 200.

[2] P. Liao, X. Zhao, G. Li, Y. Shen, M. Wang, *Nanomicro Lett* **2018**, DOI 10.1007/s40820-017-0159-z.

[3] Y.-Y. Zhang, J.-L. Xu, J.-Y. Zhang, Y. Yuan, X. Gao, S.-D. Wang, *IEEE Electron Device Letters* **2021**, *42*, 1200.

[4] R. Ollearo, A. Caiazzo, J. Li, M. Fattori, A. J. J. M. van Breemen, M. M. Wienk, G. H. Gelinck, R. A. J. Janssen, *Advanced Materials* **2022**, *34*, DOI 10.1002/adma.202205261.

[5] F. Li, Z. Qiu, S. Liu, H. Zhang, *ACS Appl Nano Mater* **2019**, *2*, 4974.

[6] Y. Wang, X. Zhang, Q. Jiang, H. Liu, D. Wang, J. Meng, J. You, Z. Yin, *ACS Appl Mater Interfaces* **2018**, *10*, 6505.

[7] W. Zhu, M. Deng, D. Chen, Z. Zhang, W. Chai, D. Chen, H. Xi, J. Zhang, C. Zhang, Y. Hao, *ACS Appl Mater Interfaces* **2020**, *12*, 32961.

[8] L. Wang, X. Zou, J. Lin, J. Jiang, Y. Liu, X. Liu, X. Zhao, Y. F. Liu, J. C. Ho, L. Liao, *ACS Nano* **2019**, *13*, 4804.

[9] Y. Wang, X. Zhang, Q. Jiang, H. Liu, D. Wang, J. Meng, J. You, Z. Yin, *ACS Appl Mater Interfaces* **2018**, *10*, 6505.

[10] R. Li, Y. Xu, W. Li, Y. Li, J. Peng, M. Xu, Q. Lin, *J Phys Chem Lett* **2021**, *12*, 1726.

[11] W. Zhu, M. Deng, D. Chen, Z. Zhang, W. Chai, D. Chen, H. Xi, J. Zhang, C. Zhang, Y. Hao, *ACS Appl Mater Interfaces* **2020**, *12*, 32961.

[12] J. M. Kim, D. H. Shin, S.-H. Choi, *Nanotechnology* **2018**, *29*, 425203.

[13] X. Huang, H.-T. Sun, N. Shirahata, *Nanotechnology* **2024**, *35*, 035701.

[14] M. Sulaman, S. Yang, Y. Jiang, Y. Tang, B. Zou, *Nanotechnology* **2017**, *28*, 505501.

[15] M. Sulaman, S. Y. Yang, Z. H. Zhang, A. Imran, A. Bukhtiar, Z. H. Ge, Y. Tang, Y. R. Jiang, L. B. Tang, B. S. Zou, *Materials Today Physics* **2022**, *27*, 100829.

[16] M. Sulaman, Y. Song, S. Yang, M. I. Saleem, M. Li, C. Perumal Veeramalai, R. Zhi, Y. Jiang, Y. Cui, Q. Hao, B. Zou, *ACS Appl Mater Interfaces* **2020**, *12*, 26153.

[17] Z. Huang, Y. Bai, X. Huang, J. Li, Y. Wu, Y. Chen, K. Li, X. Niu, N. Li, G. Liu, Y. Zhang, H. Zai, Q. Chen, T. Lei, L. Wang, H. Zhou, *Nature* **2023**, *623*, 531.

[18] S. Zeiske, W. Li, P. Meredith, A. Armin, O. J. Sandberg, *Cell Rep Phys Sci* **2022**, *3*, 101096.